Unconventional unidirectional magnetoresistance in heterostructures of a topological semimetal and a ferromagnet

I-Hsuan Kao ⓘ[1], Junyu Tang ⓘ[2], Gabriel Calderon Ortiz[3], Menglin Zhu[3], Sean Yuan[1], Rahul Rao[4], Jiahan Li ⓘ[5], James H. Edgar ⓘ[5], Jiaqiang Yan[6,7], David G. Mandrus ⓘ[6,7], Kenji Watanabe ⓘ[8], Takashi Taniguchi ⓘ[9], Jinwoo Hwang[3], Ran Cheng ⓘ[2,10,11], Jyoti Katoch ⓘ[1] & Simranjeet Singh ⓘ[1] ✉

Unidirectional magnetoresistance (UMR) in a bilayer heterostructure, consisting of a spin-source material and a magnetic layer, refers to a change in the longitudinal resistance on the reversal of magnetization and originates from the interaction of non-equilibrium spin accumulation and magnetization at the interface. Since the spin polarization of an electric-field-induced non-equilibrium spin accumulation in conventional spin-source materials is restricted to be in the film plane, the ensuing UMR can only respond to the in-plane component of magnetization. However, magnets with perpendicular magnetic anisotropy are highly desired for magnetic memory and spin-logic devices, whereas the electrical read-out of perpendicular magnetic anisotropy magnets through UMR is critically missing. Here we report the discovery of an unconventional UMR in the heterostructures of a topological semimetal (WTe_2) and a perpendicular magnetic anisotropy ferromagnetic insulator ($Cr_2Ge_2Te_6$), which allows to electrically read the up and down magnetic states of the $Cr_2Ge_2Te_6$ layer through longitudinal resistance measurements.

Electrical read-out of magnetic states is one of the key functionalities of spintronics devices to realize magnetic-based computing and data storage technologies. Since the discovery of the giant magnetoresistance and its tunnelling counterpart[1–3], which led to the development of magnetic data storage devices, other magnetoresistance effects have been experimentally observed in magnetic heterostructures to electrically read the magnetic states[4–7]. Unidirectional magnetoresistance (UMR) is a change in the longitudinal resistance of a heterostructure, composed of a spin-source material and a magnetic layer, due to

magnetization reversal and its interaction with non-equilibrium spin accumulation[6,8–14]. A change in longitudinal resistance associated with UMR, R_{UMR}, phenomenologically obeys $R_{UMR} \propto (\mathbf{m} \cdot \boldsymbol{\sigma})J$, where J is the applied charge current density, $\boldsymbol{\sigma}$ is the spin polarization generated by the inverse spin-galvanic effect in the spin-source material[15–17] and $\mathbf{m}$ specifies the magnetization direction. Distinct from other magnetoresistance effects, UMR features linear dependence on both J and $\mathbf{m}$; thus, it can monitor the magnetic state. Furthermore, UMR is finite only when the spin polarization has a component collinear with the

[1]Department of Physics, Carnegie Mellon University, Pittsburgh, PA, USA. [2]Department of Physics and Astronomy, University of California, Riverside, CA, USA. [3]Department of Materials Science and Engineering, The Ohio State University, Columbus, OH, USA. [4]Materials and Manufacturing Directorate, Air Force Research Laboratory, Wright-Patterson Air Force Base, Dayton, OH, USA. [5]Tim Taylor Department of Chemical Engineering, Kansas State University, Manhattan, KS, USA. [6]Materials Science and Technology Division, Oak Ridge National Laboratory, Oak Ridge, TN, USA. [7]Department of Materials Science and Engineering, The University of Tennessee, Knoxville, TN, USA. [8]Research Center for Electronic and Optical Materials, National Institute for Materials Science, Tsukuba, Japan. [9]Research Center for Materials Nanoarchitectonics, National Institute for Materials Science, Tsukuba, Japan. [10]Department of Electrical and Computer Engineering, University of California, Riverside, CA, USA. [11]Department of Material Science and Engineering, University of California, Riverside, CA, USA. ✉e-mail: simranjs@andrew.cmu.edu

magnetization, that is, $\mathbf{m} \cdot \boldsymbol{\sigma} \neq 0$. In conventional spin-source materials, such as heavy metals and topological insulators, a charge current applied in the film plane (for example, $\mathbf{J} \parallel \hat{\mathbf{x}}$) can only generate a spin accumulation polarized in plane and transverse to the charge current, that is, $\boldsymbol{\sigma} \parallel \hat{\mathbf{y}}$ (refs. [18–22]). Consequently, UMR in prevailing heterostructures is limited to the form of $R_{UMR} \propto (\mathbf{m} \cdot \hat{\mathbf{y}})J \propto (m_y)J$ and, thus, cannot be used to read out-of-plane oriented states of a ferromagnet with perpendicular magnetic anisotropy (PMA). Nonetheless, PMA magnets are highly desired for magnetic memory and spin-logic devices to realize ultrafast operation, thermally stable nanometre-sized magnetic bits and achieving attojoule-class logic gates. In this regard, the key to achieve a writing operation is to utilize the spin–orbit torque (SOT)-driven magnetic switching, where an out-of-plane magnetization can be efficiently manipulated by the SOT originating from the non-equilibrium spin accumulation generated in a nearby spin-source layer[18–21,23]. However, SOT-based planar magnetic memory devices considered so far mainly rely on a three-terminal configuration[19,23], where a magnetic tunnel junction is integrated on top of the spin-source material to read the magnetic state through tunnel magnetoresistance, featuring operational separation between the read and write circuits, which critically affect the footprint of individual memory nodes. Currently, an SOT-based two-terminal magnetic memory device, like commercially available magnetic-tunnel-junction-based magnetic memory devices, is missing due to the lack of identified magnetoresistance phenomena to distinguish the states of a PMA magnet in bilayer heterostructures[18,19]. We note that a two-terminal SOT switching device has been previously demonstrated by using the current-in-plane giant magnetoresistance effect in trilayer heterostructures[24,25] and by optimizing the distribution of charge current flowing through an ultrathin SOT layer integrated with a magnetic tunnel junction stack[26,27], but such a device based on purely bilayer heterostructure is still missing.

Here we report the experimental demonstration of an unconventional UMR in bilayer heterostructures consisting of WTe$_2$ (ref. [28]) and Cr$_2$Ge$_2$Te$_6$ (CGT)[29,30], allowing us to electrically read the up and down states of the magnetic layer through longitudinal resistance measurements. WTe$_2$ is believed to be a type-II Weyl semimetal[31] whose T$_d$ phase has a crystal structure with broken mirror symmetry in the a–c plane (Fig. 1a), which allows for the generation of non-equilibrium spin accumulation with a substantial out-of-plane spin polarization (σ_z) driven by a charge current applied along the crystallographic a axis (Fig. 1b, left) owing to the inverse spin-galvanic effect[15–17,32,33]. The interactions between σ_z in WTe$_2$ and magnetization in CGT gives rise to a UMR (Fig. 1b, right), enabling the distinction of up and down magnetic states via longitudinal resistance measurements, that is, lower (higher) resistance when $\mathbf{m}$ and σ_z are parallel (antiparallel). We first present our experimental results and then provide a theoretical interpretation based on a minimal tight-binding model calculation, shedding light on the microscopic origin of the observed unconventional UMR.

For our experiments, we use devices consisting of the heterostructures of atomically thin WTe$_2$ flakes (few layers) and CGT (10–15 nm) (Methods and Supplementary Notes 1 and 2). Here we present the experimental data from three samples: device A (two-layer WTe$_2$), device B (three-layer WTe$_2$) and a control sample (device C). The optical micrograph of device A is shown in Fig. 1c (bottom) along with a side-view schematic of a typical device (top). The flake thicknesses are confirmed by a combination of optical contrast and atomic force microscopy (AFM) images. The bilayer WTe$_2$ flake used in device A is shown in Fig. 1c (inset), where the thickness is confirmed by AFM (Fig. 1f). The normalized Raman peak intensity at 163 cm^{-1}, plotted against the incident laser's polarization angle relative to the current electrodes (Fig. 1d), peaks at around 0°, which indicates that the a axis of WTe$_2$ in device A aligns with the electrodes[33]. We characterized the atomic structure of the measured WTe$_2$–CGT devices using scanning transmission electron microscopy (STEM). Figure 1e shows the STEM cross-sectional image of device B (three-layer WTe$_2$ and 13.2-nm CGT),

revealing a clean, sharp WTe$_2$–CGT interface. The crystallographic orientation of WTe$_2$ in all the measured devices is confirmed by polarized Raman spectroscopy and STEM (Supplementary Note 2). Also, the resistance of individual CGT flakes at low temperature is orders of magnitude larger compared with the resistance of the WTe$_2$–CGT heterostructure, as confirmed in a control device (Fig. 1g and Supplementary Note 3), indicating that most of the current in WTe$_2$–CGT heterostructures flows through the WTe$_2$ layer.

In our devices, the electrostatic gate voltage is used to tune the electron chemical potential of WTe$_2$. The longitudinal resistance (R_{xx}) for device A as a function of the top-gate voltage (V_g) at 10 K is shown in Fig. 2a, where R_{xx} increases with increasing V_g, indicating that the bilayer WTe$_2$ is probably hole doped due to charge transfer across the interface. The hysteresis in R_{xx} (V_g) is indicative of ferroelectricity in WTe$_2$, as previously reported[34,35]. First, we discuss the experimental observation of the anomalous Hall effect (AHE) in the WTe$_2$–CGT system. Figure 2b shows the Hall resistance (R_{yx}) as a function of the out-of-plane magnetic field (B_z) in device A at different V_g values. The observed saturation in R_{yx} at $\pm B_z$ agrees well with the magnetic characteristics of CGT, that is, magnetization saturation at around $B_z \approx 50$ mT with negligible coercivity[30]. By defining $R_{yx} = \Delta R_{AHE} m_z$, where ΔR_{AHE} is the change in AHE resistance, we extract ΔR_{AHE} as a function of V_g (Fig. 2c). The magnitude of ΔR_{AHE} is strongly suppressed (enhanced) by positive (negative) V_g, consistent with our theoretical calculations in which the AHE is suppressed with an increasing electron chemical potential around the edge of the valence band (Supplementary Note 9). Next, we perform AHE hysteresis loop measurements at $V_g = 0$ for various temperatures to obtain the temperature dependence of ΔR_{AHE} (Fig. 2d), where the AHE signal vanishes near the Curie temperature of CGT ($T_C \approx 60$ K), showing that the observed AHE is due to magnetism in CGT[29] (Supplementary Note 7). Figure 2e (top) shows the AHE hysteresis loops in device B with positive and negative currents applied, where ΔR_{AHE} is independent of current polarity, as expected for a linear voltage response to the current ($V_{AHE} = \Delta R_{AHE} I$). In Fig. 2e (bottom), we calculate the symmetric (antisymmetric) part of the Hall resistance in the current polarity as follows: $R_{yx}^{symm(asym)} = \frac{R_{yx}(+I_{d.c.}) \pm R_{yx}(-I_{d.c.})}{2}$. Here R_{yx}^{symm} isolates the AHE response from the potential nonlinear thermal contribution irrelevant to AHE. The R_{yx}^{asym} value evidently shows a negligible non-AHE response. Device B also shows the hole-doped transport and ferroelectricity (Fig. 2f, inset), although a lower resistance due to the three layers of WTe$_2$ and a gate-voltage-dependent ΔR_{AHE} (Fig. 2f), that is, the suppression of AHE at positive V_g, are observed. The observed AHE can originate due to the magnetic proximity effects in WTe$_2$ (refs. [7,36–38]), for example, the Berry curvature induced by an exchange interaction from the magnetization of CGT.

Next, we present the experimental realization of unconventional UMR in WTe$_2$–CGT heterostructures to electrically read the out-of-plane magnetization of CGT. As shown in Fig. 3a, when a positive charge current is applied along the a axis of WTe$_2$ in device A, there is a clear step in resistance, proportional to m_z, in the raw longitudinal resistance (R_{xx}^{raw}) as a function of B_z, indicating the presence of unconventional UMR. By considering the saturated branches at high field (>100 mT), we model the longitudinal resistance by considering $R_{xx}^{raw} = \Delta R_{UMR} m_z + R_{xx,\alpha} B_z^2 + R_{xx,\beta} B_z + R_0$, where ΔR_{UMR} is the UMR resistance, $R_{xx,\alpha}$ ($R_{xx,\beta}$) is the parameter for quadratic (linear) B_z dependence and R_0 is the field-independent component of the longitudinal resistance. The quadratic B_z dependence arises from ordinary magnetoresistance, whereas the slight linear correction stems from the ordinary Hall effect due to the non-uniform flake width. Figure 3b shows the longitudinal resistance R_{xx}, after excluding effects other than UMR, with a positive and negative current applied, where ΔR_{UMR} switches sign with the current polarity reversal, as expected for a nonlinear response. We extract the symmetric (antisymmetric) part of R_{xx} with respect to the current polarity, as follows: $R_{xx}^{symm(asym)} = \frac{R_{xx}(+I_{d.c.}) \pm R_{xx}(-I_{d.c.})}{2}$. As expected, UMR, due to its unidirectional nature, is negligible in R_{xx}^{symm}.
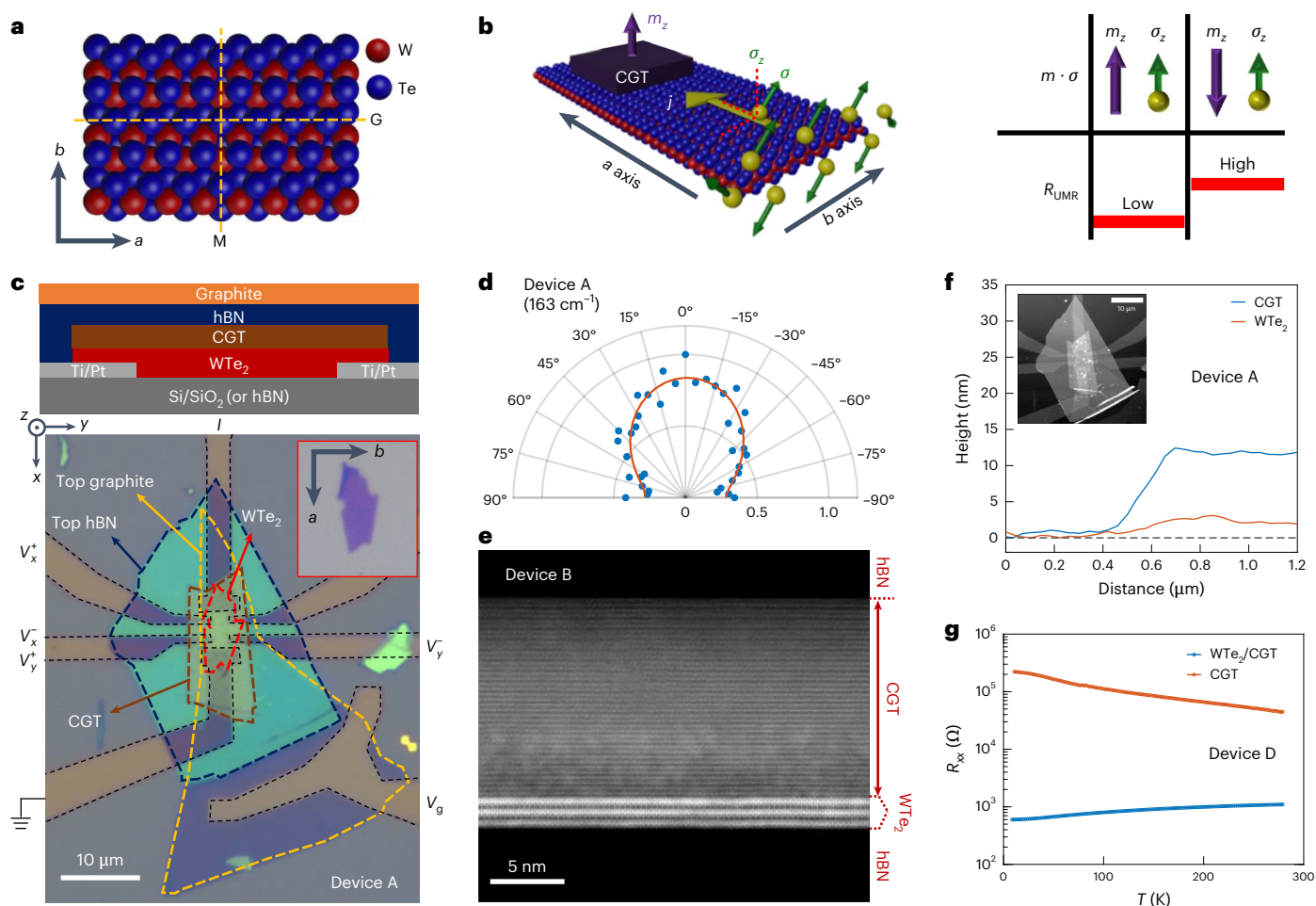
Fig. 1 | WTe₂–CGT devices and their characterization. a, A model showing the crystal structure of WTe₂ with the a axis and b axis labelled. The crystal is invariant (non-invariant) under a b–c (a–c) mirror operation. The mirror (M) and glide (G) planes are indicated by yellow dashed lines. **b**, Left: schematic showing the generation of non-equilibrium spin accumulation with an out-of-plane spin polarization (σ_z), when a charge current (J) is applied along the a axis of WTe₂. Right: schematic depicting the concept of unconventional UMR in heterostructures, that is, change in longitudinal resistance (R_{UMR}) depending on the relative orientation of out-of-plane magnetization (m_z) and spin polarization (σ_z). When the magnetization is parallel (antiparallel) to the spin polarization, R_{UMR} is negative (positive), leading to a low-resistance (high-resistance) state.

c, Top: schematic showing the side view of a typical device. Bottom: optical image of device A with the a axis of WTe₂ aligned along the current electrodes, with CGT, WTe₂, graphite and hBN flakes outlined and labelled. The Pt electrodes are outlined with dashed black lines. Inset: optical image of the WTe₂ flake used in device A. **d**, Angle-dependent polarized Raman spectral intensity at 163 cm⁻¹ of the WTe₂ flake used in device A. **e**, Cross-sectional STEM image of the WTe₂–CGT device B as viewed along the crystallographic b axis of WTe₂. **f**, AFM line scan at the edges of the flakes, reflecting the thickness of WTe₂ and CGT. Inset: full topography map obtained by AFM. **g**, Two-point longitudinal resistance as a function of temperature measured in a single device (device D) having a WTe₂–CGT region (blue curve) and a CGT region (orange).

The small peaks in R_{xx}^{symm} are probably due to a linear magnetoresistance effect proportional to $(\mathbf{m} \cdot \boldsymbol{\sigma})^2$ because of band modulation induced by exchange interactions from the magnetization in CGT[6]. Next, we focus on UMR by showing R_{xx}^{asym} as a function of B_z in device A at various V_g values (Fig. 3c). We extract ΔR_{UMR} as a function of V_g (Fig. 3d), which clearly shows that ΔR_{UMR} is enhanced (suppressed) at positive (negative) V_g, consistent with our theoretical calculations in which UMR is enhanced with an increasing electron chemical potential around the edge of the valence band. Next, UMR measurements are performed at various temperatures (Supplementary Note 7) to obtain the temperature dependence of ΔR_{UMR} (Fig. 3e). As expected, ΔR_{UMR} reduces as the temperature approaches T_C of CGT, indicating that the observed UMR is indeed due to the magnetic coupling between WTe₂ and CGT magnetization. Next, we examine the current dependence of UMR (Fig. 3f) by extracting the $\Delta R_{UMR}^{+/-}$ values at various current magnitudes ($|I_{d.c.}|$), where $\Delta R_{UMR}^{+/-}$ is the ΔR_{UMR} value measured at a positive/negative current (Supplementary Note 6). The measured UMR scales with the current in the low-current region, whereas in the higher-current region, it shows

a deviation from linear behaviour, probably due to the increase in temperature in CGT caused by Joule heating. For device B, with three layers of WTe₂, when a charge current is applied along the a axis, the R_{xx}^{raw} value as a function of B_z is shown in Fig. 3g. The extracted $R_{xx}^{asym/symm}$ value in device B (Fig. 4h) shows the UMR results, which are consistent with the UMR data obtained for device A. Finally, the ΔR_{UMR} value in device B shows a gate-voltage dependence (like device A), where UMR is suppressed by the negative gate voltage. Note that ΔR_{UMR} is negative in device B, as the UMR sign depends on whether the positive-current direction is along $+\hat{\mathbf{a}}$ or $-\hat{\mathbf{a}}$ of WTe₂. The UMR in devices A and B is of the same order of magnitude when plotted as a percentage change versus the charge current density (Fig. 4f), accounting for the thickness-dependent resistance of WTe₂ (Supplementary Note 3).

By contrast, magnetoresistance is expected to be completely different when current is applied along the b axis, that is, UMR due to the out-of-plane magnetization should vanish due to the absence of σ_z. To examine this, we prepare control device C (Fig. 4a), consisting of three-layer WTe₂ and 8.1-nm CGT, with the b axis aligned to the current
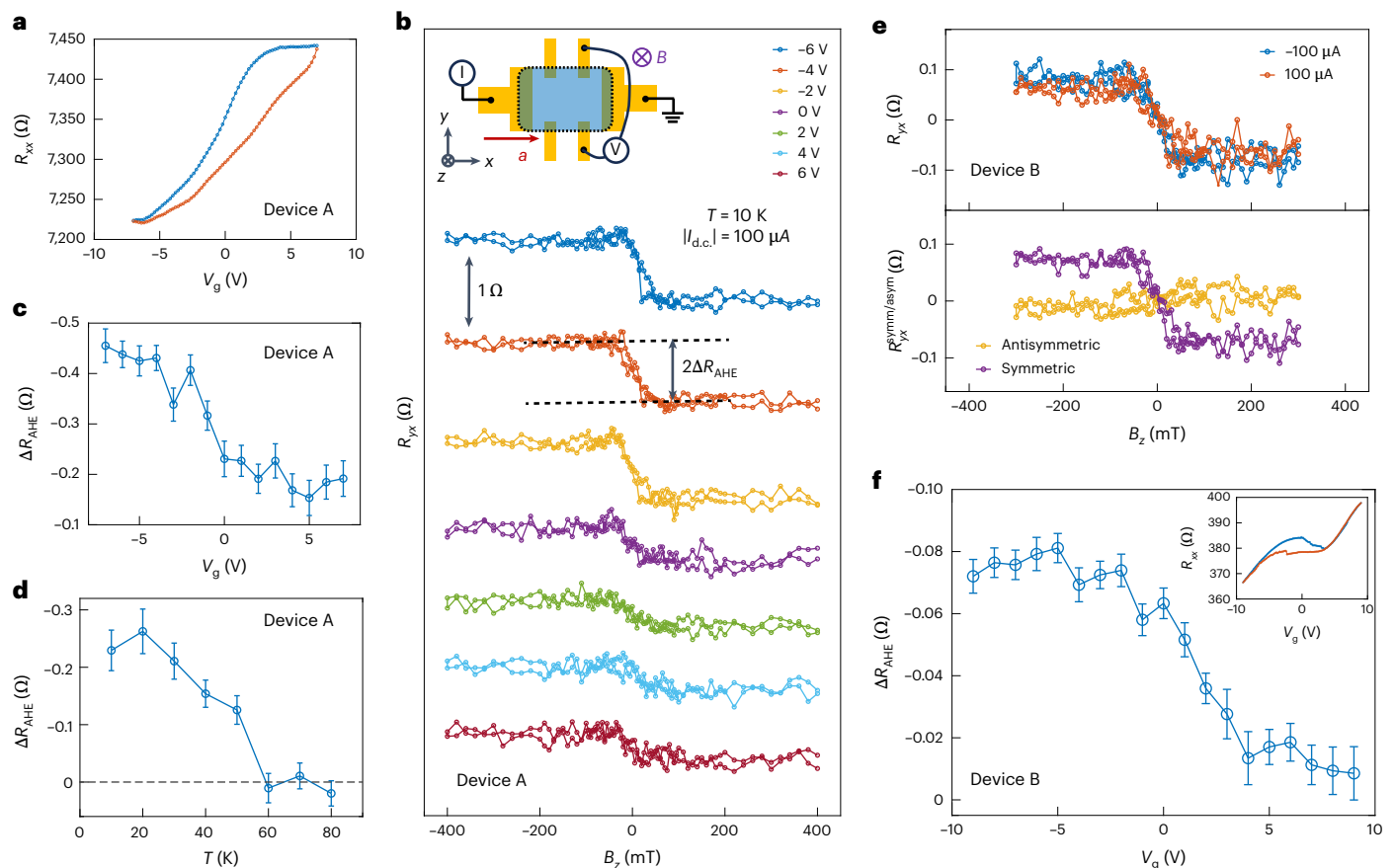
Fig. 2 | AHE in WTe$_2$–CGT devices. a, Two-point longitudinal resistance (R_{xx}) as a function of gate voltage (V_g) measured in device A. The hysteresis in R_{xx} is probably due to the ferroelectric behaviour of WTe$_2$. **b**, AHE hysteresis loops (R_{yx} versus B_z), measured at 10 K at various V_g values when a charge current of $|I_{d.c.}| = 100$ μA is applied along the a axis in device A. Inset: schematic showing the configuration for the transverse-resistance (R_{yx}) measurement. **c**, Measured AHE resistance (ΔR_{AHE}) as a function of V_g at 10 K. **d**, ΔR_{AHE} measured at $V_g = 0$ as a function of the sample temperature. **e**, Top: AHE hysteresis loops measured in device B at +100 μA (−100 μA) are shown as the orange (blue) curve, depicting no

notable difference on reversing the charge current polarity. Bottom: antisymmetric part (R_{yx}^{asym}) and symmetric part (R_{yx}^{symm}) of the transverse resistance are plotted as the yellow and purple curves, respectively. **f**, Obtained ΔR_{AHE} as a function of V_g when a charge current of $|I_{d.c.}| = 100$ μA is applied along the a axis in device B at 10 K. Inset: R_{xx} as a function of V_g in device B, with a similar hysteresis loop as observed in the other device. ΔR_{AHE} in **c**, **d** and **f** are the fitted results using linear least squares with more than 60 data points and 4 fitting parameters, whereas the error bars represent the 95% confidence intervals.

electrodes (confirmed by polarized Raman spectroscopy; Fig. 4b). The $R_{xx}(V_g)$ value in device C (Fig. 4c) shows hole-doped and ferroelectricity characteristics (like devices A and B). The measured R_{yx} value as a function of B_z in device C at various V_g values (Fig. 4d) depicts a clear AHE, indicating that the AHE is independent of whether current is applied along the a or b axis. In striking contrast, R_{xx}^{asym} as a function of B_z at various V_g values measured in device C (Fig. 4e) shows no signature of UMR when the current is applied along the b axis. To better compare the UMR in WTe$_2$–CGT devices, we plot the normalized UMR, that is, $|\Delta R_{UMR}/R_0|$ as a function of the charge current density $|J_{d.c.}|$, and the results from three measured devices are shown in Fig. 3f. For the control device (device C), the normalized UMR remains zero within the experimental measurement limits as a function of $|J_{d.c.}|$ applied along the b axis. Conversely, the normalized UMR scales linearly with $|J_{d.c.}|$ in devices A and B, which distinctly suggests that the unconventional UMR in these devices is due to the presence of σ_z, which is only allowed when a charge current is applied along the low-symmetry axis, that is, a axis, in WTe$_2$.

Such a nonlinear magnetoresistance can also be induced by a thermal gradient due to Joule heating in the form of $|\nabla T| \propto I^2$ through thermoelectric effects such as the anomalous Nernst effect and spin Seebeck effect[39,40]. The electric field due to thermoelectric effects has the form of $\mathbf{E}_{TE} \propto \mathbf{m} \times \nabla T$; therefore, to observe a change in R_{xx} for

out-of-plane magnetization, it requires an in-plane thermal gradient (y direction). We will provide three pieces of evidence to show that the thermoelectric effects are not dominant in our system compared with the unconventional UMR. First, if the measured magnetization-dependent nonlinear resistance signal is due to thermoelectric effects, one would expect a similar magnetoresistance when the current is applied along the b axis. However, no signature of UMR associated with perpendicular magnetization is observed when current is applied along the b axis ($\mathbf{I} \parallel \hat{\mathbf{b}}$) in the control device (Fig. 4e), consistent with the fact that σ_z is absent when $\mathbf{I} \parallel \hat{\mathbf{b}}$. Second, in our devices, the WTe$_2$ layer conducts most of the current, and the thermal gradient is mostly out of plane, and thus, the in-plane thermal gradient is expected to be small[40]. Finally, if there is a small y-direction thermal gradient in our system, it should point in opposite directions at the two opposite edges of WTe$_2$ since the in-plane ∇T should be roughly normal to the edge of the conducting region and pointing outwards, that is, towards the voltage probes. This will result in a sign change of such magnetoresistance when the voltage probes on the opposite sides of the flakes are used for longitudinal resistance measurements. We have measured unconventional UMR using voltage probes on opposite sides in device A and UMR is of the same sign and similar magnitude (Supplementary Note 4). Thus, our experiments unequivocally rule out the thermoelectric-effects-related origin of UMR and suggest that the
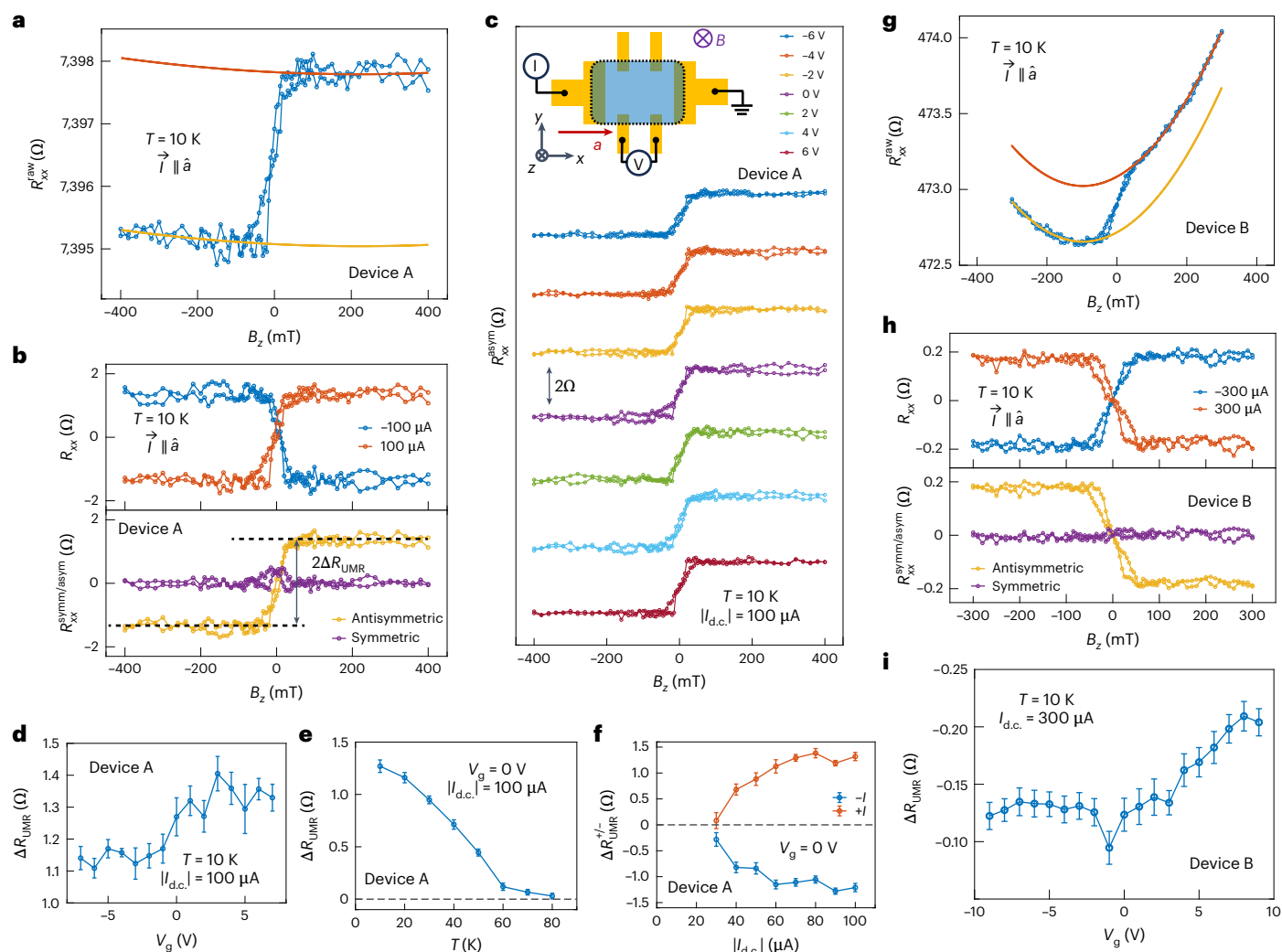
Fig. 3 | Unconventional UMR in WTe$_2$–CGT devices. a, Raw longitudinal resistance (R_{xx}^{raw}) signal measured as a function of out-of-plane magnetic field (B_z) when a positive charge current of 100 µA is applied along the a axis in device A at 10 K. The orange (yellow) lines are fit to the saturated region at a positive (negative) magnetic field side to subtract the background not associated with UMR. **b**, Top: obtained R_{xx} after subtracting a trivial background at saturated magnetization regions under positive (orange curve) and negative (blue curve) charge currents. Bottom: antisymmetric part (R_{xx}^{asym}) and symmetric part (R_{xx}^{symm}) of the longitudinal resistance are obtained and plotted as the yellow and purple curves, respectively. **c**, R_{xx} versus B_z hysteresis loops, associated with unconventional UMR, are measured at 10 K at various V_g values. Inset: schematic depicting the configuration for R_{xx} versus B_z measurements. **d**, Magnitude of UMR (ΔR_{UMR}), as defined in **b** (bottom), is plotted as a function of V_g at 10 K. **e**, ΔR_{UMR} as a function of temperature with a charge current of $|I_{\text{d.c.}}| = 100$ µA and

$V_g = 0$ V. **f**, Magnitude of the measured UMR at positive (orange curve) and negative (blue curve) charge currents, that is, $\Delta R_{\text{UMR}}^{+/-}$, as a function of the charge current magnitude ($|I_{\text{d.c.}}|$) in device A at 10 K. **g**, Measured R_{xx}^{raw} as a function of B_z when a negative charge current of -300 µA is applied along the a axis in device B. The orange (yellow) curve is fit to the background in the saturated region at the positive-field (negative-field) side. **h**, Top: obtained R_{xx} after subtracting a trivial background in the saturated magnetization regions shown in **g**, at positive (orange curve) and negative (blue curve) charge currents. Bottom: R_{xx}^{asym} and R_{xx}^{symm} as a function of B_z, obtained from the top panel, are plotted as the yellow and purple curves, respectively. **i**, Obtained ΔR_{UMR} as a function of V_g at 10 K when a charge current of $|I_{\text{d.c.}}| = 300$ µA is applied. ΔR_{UMR} in **d**, **e** and **i** and $\Delta R_{\text{UMR}}^{\pm}$ in **f** are the fitted results using linear least squares with more than 60 data points and 4 fitting parameters, whereas the error bars represent the 95% confidence intervals.

origin of the observed unconventional UMR is related to the intrinsic spin-dependent electron conduction affected by the exchange coupling interactions.

To understand unconventional UMR, we theoretically model the magnetotransport in the WTe$_2$–CGT heterostructure. In the following, an electric field is assumed to be applied in the x direction, but the results can be generalized to arbitrary directions. With the longitudinal resistivity defined as $\rho_{xx}(E_x) = E_x/j_x(E_x)$, the UMR ratio can be written as

$$\text{UMR} = \frac{\rho_{xx}(E_x) - \rho_{xx}(-E_x)}{\rho_{xx}(E_x) + \rho_{xx}(-E_x)} = -\frac{j_x(E_x) + j_x(-E_x)}{j_x(E_x) - j_x(-E_x)}. \quad (1)$$

If there is no asymmetry in the charge current for the $\pm E_x$ field, that is, $j_x(-E_x) = -j_x(E_x)$, then the UMR vanishes, indicating that the UMR inherently belongs to the nonlinear longitudinal response. For the second order in E_x, the current can be expanded as

$$j_x(E_x) = j_x^{(1)} + j_x^{(2)} = \sigma_{xx}^{(1)}E_x + \sigma_{xx}^{(2)}(E_x)^2 + \dots. \quad (2)$$

The second-order conductivity $\sigma_{xx}^{(2)}$ introduces a nonlinear charge current $j_x^{(2)} \approx E_x^2$, remaining invariant after reversing E_x, leaving an asymmetric longitudinal response $j_x(E_x) \neq j_x(-E_x)$ interpreted as the UMR. For the case of $j_x^{(1)} \gg j_x^{(2)}$, UMR defined in equation (1) is approximately the normalized UMR, that is, $|\Delta R_{\text{UMR}}/R_0|$ in the
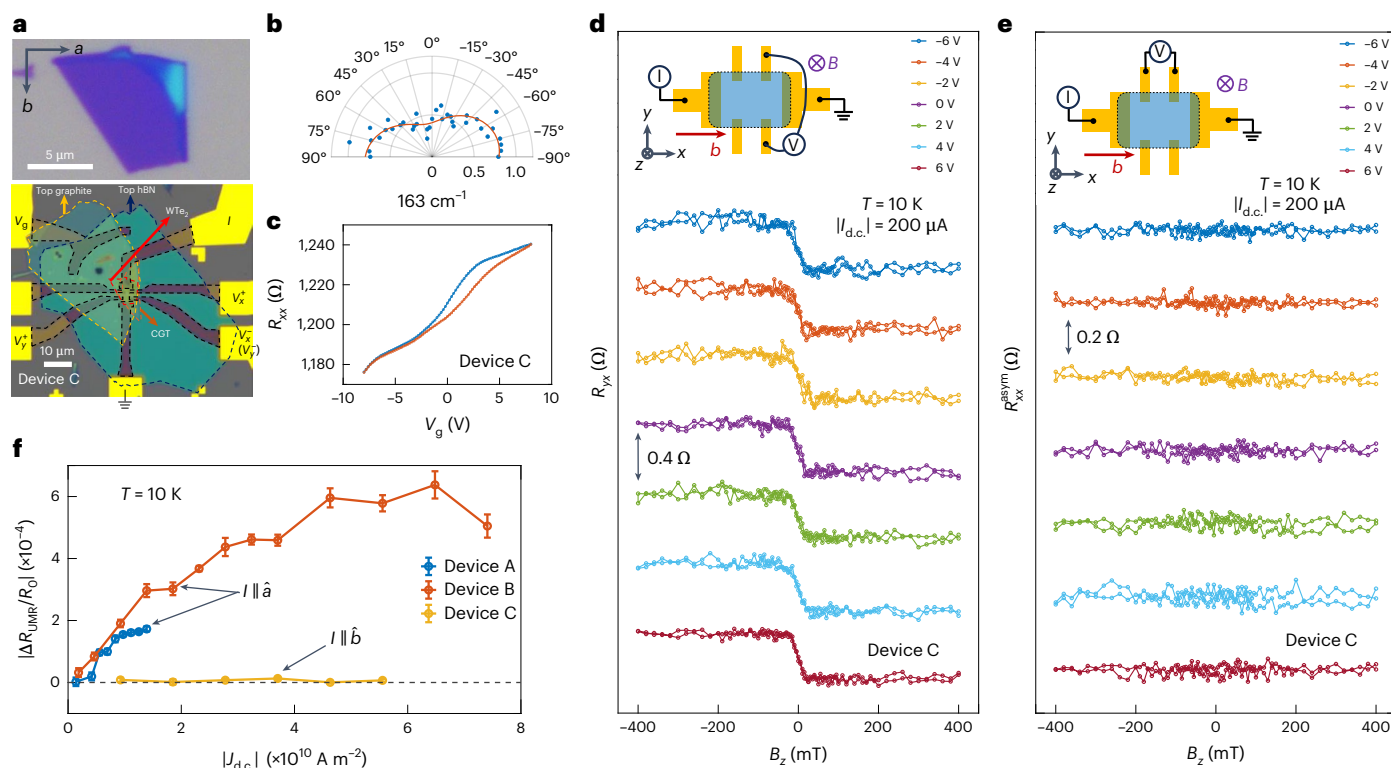
Fig. 4 | Absence of unconventional UMR in control device. a, Top: optical image of the WTe$_2$ flake used in device C, with the a-axis and b-axis orientations labelled. Bottom: optical image of device C with the b axis of WTe$_2$ aligned with the current electrodes, with the flake of CGT, WTe$_2$, graphite and hBN outlined and labelled. The Pt electrodes are outlined with the dashed black lines. **b**, Angle-dependent polarized Raman spectral intensity at 163 cm^{-1} of WTe$_2$ flake (as shown in **a**) used in device C, confirming that the b axis of the WTe$_2$ flake is aligned parallel to the current electrodes. **c**, Measured R_{xx} as a function of V_g in device C at 10 K showing hysteresis, which is probably due to ferroelectric switching in WTe$_2$. **d**, AHE hysteresis loops (R_{yx} versus B_z), measured at 10 K at V_g when a charge current of $|I_{d.c.}| = 200$ μA is applied along the b axis in device C and the magnetic field is applied in the out-of-plane direction. Inset: schematic showing the configuration

for R_{yx} versus B_z measurements. **e**, Obtained antisymmetric longitudinal resistance (R_{xx}^{asym}) hysteresis loops at various V_g values when a charge current of $|I_{d.c.}| = 200$ μA is applied along the b axis in device C at 10 K shows no signature of the presence of unconventional UMR. Inset: schematic depicting the configuration for R_{xx} versus B_z measurements. **f**, Obtained normalized UMR magnitude ($|\Delta R_{UMR}/R_0|$), where R_0 is the magnetic-field-independent part of the longitudinal resistance, as a function of the charge current density magnitude $|J_{d.c.}|$ in devices A, B and C. A linear current density dependence of normalized UMR is only observed in devices A and B, where the current is applied along the a axis of WTe$_2$. $|\Delta R_{UMR}/R_0|$ in **f** is the fitted result using linear least squares with more than 60 data points and 4 fitting parameters, whereas the error bars represent the 95% confidence intervals.

experimental results. Inserting equation (2) into equation (1), UMR arrives at a simple relation:

$$UMR \approx -\frac{\sigma_{xx}^{(2)}}{\sigma_{xx}^{(1)}}E_x. \tag{3}$$

The microscopic origin of σ_z in WTe$_2$ can be attributed to the layered spin Edelstein effect, consistent with the screw-axis and glide-plane symmetries in WTe$_2$ (refs. [32,41]) (Supplementary Note 10). As the CGT is insulating, considering only the first-adjacent WTe$_2$ layer is enough for qualitatively modelling the electron transport in WTe$_2$–CGT heterostructures[11]. Additionally, a negligible UMR is expected in the bulk WTe$_2$ sample, consistent with our experimental data (Supplementary Note 5). We include an exchange coupling ($\Delta_{ex} \propto m_z$) and an interfacial Rashba SOC (α_R) into the 1T$_d$-monolayer WTe$_2$ Hamiltonian[42] (Methods and Supplementary Note 8). We first calculate the first-order conductivity for WTe$_2$–CGT heterostructures (Fig. 5a), where $\sigma_{xx}^{(1)}$ and $\sigma_{yy}^{(1)}$ are even in the exchange coupling Δ_{ex}, and the x (y) axis is defined along the a (b) axis of WTe$_2$. Comparatively, the transverse conductivities, namely, $\sigma_{xy}^{(1)}$ and $\sigma_{yx}^{(1)}$ accounting for the AHE, are odd functions of Δ_{ex}, which agree qualitatively with our experimental observations. Note that for our measured devices, a charge current density ($J_{d.c.} \approx 10^{10}$ A m^{-2}) corresponds to an

electric field, that is, $E \approx 10^5$ V m^{-1}, of the same order of E used in our calculations (Fig. 5c).

The second-order longitudinal conductivity, which accounts for UMR, vanishes if the electric field is applied along the y direction (b axis), that is, $\sigma_{yy}^{(2)} = 0$ (Fig. 5b). By contrast, a finite $\sigma_{xx}^{(2)}$ indicates that when the electric field has a finite projection along the x direction (that is, the a axis), a non-vanishing UMR appears, agreeing well with the experimental observations. UMR calculated from equation (3) as functions of B_z and E_x are plotted in Fig. 5c,d, respectively. Figure 5c shows the sign flip of UMR when B_z reverses, consistent with our experimental results. This can be understood by the sign change in Δ_{ex} (Fig. 5b) caused by the magnetization switching of CGT. Note that for $|B_z| < 50$ mT, where CGT has low remanent magnetization due to either a reduced magnetic anisotropy or multidomain formation, the results are not shown[29]. Because the magnetic field enters the WTe$_2$ Hamiltonian through Zeeman coupling, which is usually much weaker than the exchange coupling, UMR is almost independent of B_z after magnetization saturation. We also found that AHE (UMR) is suppressed (enhanced) with an increasing electron chemical potential around the edge of the valence band (Supplementary Note 9), in qualitative agreement with our gate-voltage-dependent measurements of AHE and UMR in hole-doped WTe$_2$–CGT devices. UMR can also be phenomenologically understood by symmetry considerations. Our calculation of non-equilibrium spin accumulation in the linear response to an applied electric field shows
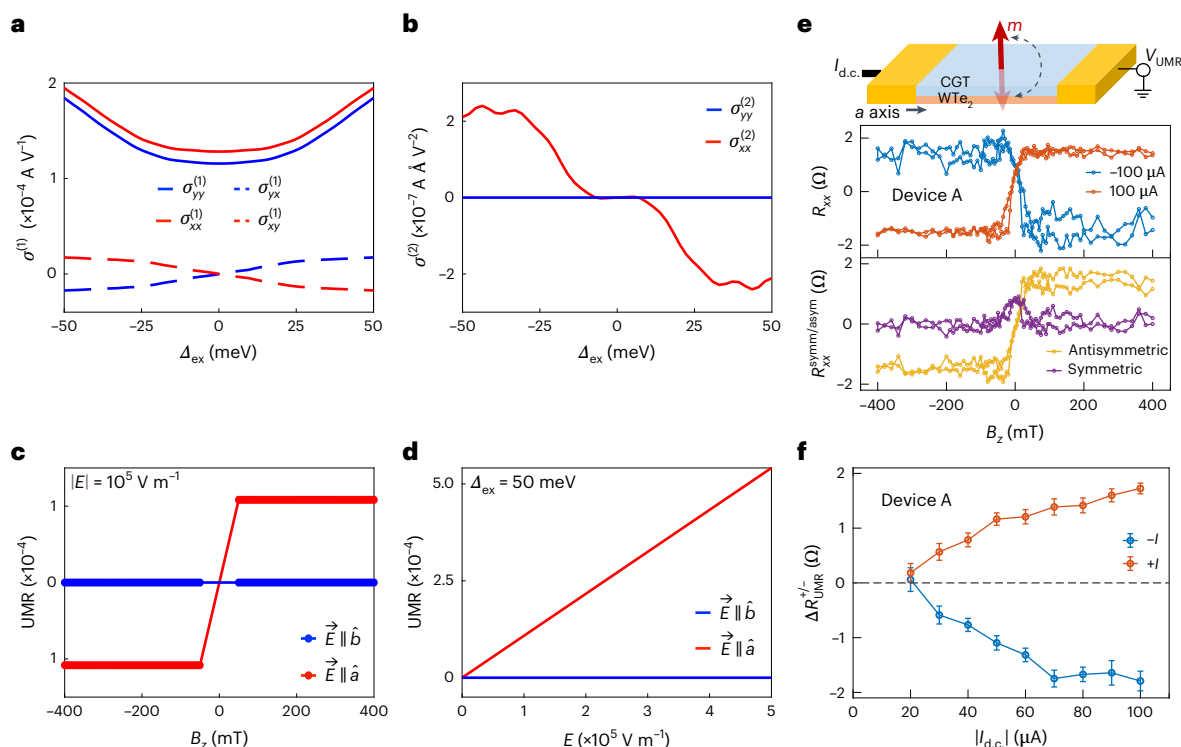
Fig. 5 | Theoretical modelling of UMR and AHE. a,b, First-order (**a**) and second-order (**b**) conductivities as a function of exchange coupling. The transverse conductivity $\sigma_{xy}^{(1)} = -\sigma_{yx}^{(1)}$ accounts for the AHE and the UMR is proportional to the second-order conductivity, that is, $\sigma_{xx}^{(2)}$ and $\sigma_{yy}^{(2)}$. **c,d,** UMR as a function of out-of-plane magnetic field B_z (**c**) and electric field E (**d**) when the electric field is applied along the a (red curve) and b (blue curve) axes of WTe$_2$. **e,** Top: schematic showing the measurement configuration to read the out-of-plane magnetic state of CGT using the two-point longitudinal resistance (R_{xx}). Middle: measured two-point R_{xx} when positive (orange curve) and negative (blue curve) charge currents are applied along the a axis of WTe$_2$ in device A. The step-like change in the two-point R_{xx} is due to the UMR switching sign when the current is reversed. Bottom: antisymmetric part (R_{xx}^{asym}) and symmetric part (R_{xx}^{symm}) of the two-point R_{xx} are plotted as the yellow and purple curves, respectively, which clearly shows that the out-of-plane magnetization of CGT can be electrically read through the UMR. **f,** Measured magnitude of UMR ($\Delta R_{\mathrm{UMR}}^{+/-}$), obtained from the two-point R_{xx} measurements, as a function of the charge current magnitude $|I_{\mathrm{d.c.}}|$ when positive (orange curve) and negative (blue curve) charge currents are applied along the a axis of WTe$_2$ in device A at 10 K. $\Delta R_{\mathrm{UMR}}^{+/-}$ in **f** is the fitted result using linear least squares with more than 60 data points and 4 fitting parameters, whereas the error bars represent the 95% confidence intervals.

that σ_z in WTe$_2$ is finite only when the electric field is along the x direction, that is, a axis (Supplementary Note 10). Consequently, with a fixed magnetization along the z direction, switching the current in the x direction reverses σ_z in WTe$_2$, subjecting it to an opposite exchange field from the CGT layer, thereby inducing asymmetric spin-dependent transport in WTe$_2$, which manifests as the UMR. Previously, a non-reciprocal magnetoelectric effect has been observed in a monolayer WTe$_2$ coupled to a layered antiferromagnet, which originated from a quantum spin Hall effect in WTe$_2$ in the presence of the magnetic proximity effect[43]. However, unconventional UMR in our devices with few-layer WTe$_2$ is not associated with helical edge states. Additionally, the spin-dependent scattering[44] and the interfacial mechanism related to the spin-magnon interaction[6,45], which exhibits a distinct temperature- and magnetic-field-dependent magnetoresistance, are not accountable for the observed unconventional UMR.

One of the outstanding challenges in spintronics research is to realize a planar two-terminal SOT-based magnetic memory device[19,23], which requires that the out-of-plane magnetic state is electrically readable through two-point measurements. So far, we have shown the UMR electrical read-out of the magnetic state of CGT using four-point longitudinal measurements. Next, we show that UMR can be used to electrically read the magnetic state of CGT using a two-point measurement configuration. We use device A and measured the UMR using a two-point configuration (Fig. 5e, top) and the obtained R_{xx} value as a function of B_z with positive and negative currents is shown in Fig. 5e (middle). The extracted R_{xx}^{asym} (Fig. 5e, bottom) clearly shows that the

perpendicular magnetization of CGT is detected by the unconventional UMR in the two-point measurements. Figure 5f shows the current dependence of ΔR_{UMR} measured in the two-point configuration in device A, in good agreement with the four-point measurement results. Note that the slightly larger UMR in the two-point method is due to the increased length of the measurement channel.

We experimentally reported the discovery of an unconventional UMR in WTe$_2$–CGT heterostructures, which enables reading the out-of-plane states of the PMA magnet through longitudinal resistance measurements. Our comprehensive experiments and theoretical modelling confirm that the observed UMR in WTe$_2$–CGT heterostructures originates from the interplay between the interfacial exchange coupling and the interfacial Rashba spin–orbit coupling, in the low-symmetry crystal structure of WTe$_2$. Our findings provide a new pathway to realize SOT-based two-terminal magnetic memory devices for the development of next-generation non-volatile and low-power-consumption data storage technologies. Given that our results are not only limited to CGT, that is, one should observe this magnetoresistance phenomena by coupling WTe$_2$ (or other spin-source materials with out-of-plane spin polarization[46]) to PMA magnets with a higher Curie temperature. Future studies to optimize unconventional UMR at room temperature will be crucial for practical device applications. Furthermore, the main ingredient for unconventional UMR, that is, an out-of-plane spin polarization, is not limited to low-symmetry spin-source materials but can also arise in thin films and bulk crystals of magnetic systems[47,48]. This opens an exciting opportunity to explore if unconventional UMR

can be observed in a wider class of material systems to enable new functionalities for spintronic devices.

Online content

Any methods, additional references, Nature Portfolio reporting summaries, source data, extended data, supplementary information, acknowledgements, peer review information; details of author contributions and competing interests; and statements of data and code availability are available at https://doi.org/10.1038/s41563-025-02175-0.

References

1. Baibich, M. N. et al. Giant magnetoresistance of (001)Fe/(001)Cr magnetic superlattices. *Phys. Rev. Lett.* **61**, 2472–2475 (1988).
2. Binasch, G., Grünberg, P., Saurenbach, F. & Zinn, W. Enhanced magnetoresistance in layered magnetic structures with antiferromagnetic interlayer exchange. *Phys. Rev. B* **39**, 4828–4830 (1989).
3. Julliere, M. Tunneling between ferromagnetic films. *Phys. Lett. A* **54**, 225–226 (1975).
4. Nakayama, H. et al. Spin Hall magnetoresistance induced by a nonequilibrium proximity effect. *Phys. Rev. Lett.* **110**, 206601 (2013).
5. Nakayama, H. et al. Rashba-Edelstein magnetoresistance in metallic heterostructures. *Phys. Rev. Lett.* **117**, 116602 (2016).
6. Yasuda, K. et al. Large unidirectional magnetoresistance in a magnetic topological insulator. *Phys. Rev. Lett.* **117**, 127202 (2016).
7. Lu, Y. M. et al. Hybrid magnetoresistance in the proximity of a ferromagnet. *Phys. Rev. B* **87**, 220409 (2013).
8. Avci, C. O. et al. Unidirectional spin Hall magnetoresistance in ferromagnet/normal metal bilayers. *Nat. Phys.* **11**, 570–575 (2015).
9. Lv, Y. et al. Unidirectional spin-Hall and Rashba–Edelstein magnetoresistance in topological insulator-ferromagnet layer heterostructures. *Nat. Commun.* **9**, 111 (2018).
10. Zhang, S. S. L. & Vignale, G. Theory of unidirectional spin Hall magnetoresistance in heavy-metal/ferromagnetic-metal bilayers. *Phys. Rev. B* **94**, 140411 (2016).
11. Shim, S. et al. Unidirectional magnetoresistance in antiferromagnet/heavy-metal bilayers. *Phys. Rev. X* **12**, 021069 (2022).
12. Duy Khang, N. H. & Hai, P. N. Giant unidirectional spin Hall magnetoresistance in topological insulator–ferromagnetic semiconductor heterostructures. *J. Appl. Phys.* **126**, 233903 (2019).
13. Lv, Y. et al. Large unidirectional spin Hall and Rashba–Edelstein magnetoresistance in topological insulator/magnetic insulator heterostructures. *Appl. Phys. Rev.* **9**, 011406 (2022).
14. Cheng, Y. et al. Unidirectional spin Hall magnetoresistance in antiferromagnetic heterostructures. *Phys. Rev. Lett.* **130**, 086703 (2023).
15. Edelstein, V. M. Spin polarization of conduction electrons induced by electric current in two-dimensional asymmetric electron systems. *Solid State Commun.* **73**, 233–235 (1990).
16. Johansson, A., Henk, J. & Mertig, I. Edelstein effect in Weyl semimetals. *Phys. Rev. B* **97**, 085417 (2018).
17. Garate, I. & Franz, M. Inverse spin-galvanic effect in the interface between a topological insulator and a ferromagnet. *Phys. Rev. Lett.* **104**, 146802 (2010).
18. Miron, I. M. et al. Perpendicular switching of a single ferromagnetic layer induced by in-plane current injection. *Nature* **476**, 189–193 (2011).
19. Liu, L. et al. Spin-torque switching with the giant spin Hall effect of tantalum. *Science* **336**, 555–558 (2012).
20. Liu, L., Lee, O. J., Gudmundsen, T. J., Ralph, D. C. & Buhrman, R. A. Current-induced switching of perpendicularly magnetized magnetic layers using spin torque from the spin Hall effect. *Phys. Rev. Lett.* **109**, 096602 (2012).
21. Mellnik, A. R. et al. Spin-transfer torque generated by a topological insulator. *Nature* **511**, 449–451 (2014).
22. Sinova, J., Valenzuela, S. O., Wunderlich, J., Back, C. H. & Jungwirth, T. Spin Hall effects. *Rev. Mod. Phys.* **87**, 1213–1260 (2015).
23. Shao, Q. et al. Roadmap of spin–orbit torques. *IEEE Trans. Magn.* **57**, 800439 (2021).
24. Avci, C. O., Lambert, C.-H., Sala, G. & Gambardella, P. A two-terminal spin valve device controlled by spin–orbit torques with enhanced giant magnetoresistance. *Appl. Phys. Lett.* **119**, 032406 (2021).
25. Damerio, S. et al. Magnetoresistive detection of perpendicular switching in a magnetic insulator. *Commun. Phys.* **7**, 114 (2024).
26. Sato, N., Xue, F., White, R. M., Bi, C. & Wang, S. X. Two-terminal spin–orbit torque magnetoresistive random access memory. *Nat. Electron.* **1**, 508–511 (2018).
27. Wang, M. et al. Field-free switching of a perpendicular magnetic tunnel junction through the interplay of spin–orbit and spin-transfer torques. *Nat. Electron.* **1**, 582–588 (2018).
28. Zhao, Y. et al. Anisotropic magnetotransport and exotic longitudinal linear magnetoresistance in WTe_2 crystals. *Phys. Rev. B* **92**, 041104 (2015).
29. Gong, C. et al. Discovery of intrinsic ferromagnetism in two-dimensional van der Waals crystals. *Nature* **546**, 265–269 (2017).
30. Wang, Z. et al. Electric-field control of magnetism in a few-layered van der Waals ferromagnetic semiconductor. *Nat. Nanotechnol.* **13**, 554–559 (2018).
31. Soluyanov, A. A. et al. Type-II Weyl semimetals. *Nature* **527**, 495–498 (2015).
32. MacNeill, D. et al. Control of spin–orbit torques through crystal symmetry in WTe_2/ferromagnet bilayers. *Nat. Phys.* **13**, 300–305 (2017).
33. Kao, I. H. et al. Deterministic switching of a perpendicularly polarized magnet using unconventional spin–orbit torques in WTe_2. *Nat. Mater.* **21**, 1029–1034 (2022).
34. Fei, Z. et al. Ferroelectric switching of a two-dimensional metal. *Nature* **560**, 336–339 (2018).
35. de la Barrera, S. C. et al. Direct measurement of ferroelectric polarization in a tunable semimetal. *Nat. Commun.* **12**, 5298 (2021).
36. Mogi, M. et al. Large anomalous Hall effect in topological insulators with proximitized ferromagnetic insulators. *Phys. Rev. Lett.* **123**, 016804 (2019).
37. Gupta, V. et al. Gate-tunable anomalous Hall effect in a 3D topological insulator/2D magnet van der Waals heterostructure. *Nano Lett.* **22**, 7166–7172 (2022).
38. Li, J. et al. Proximity-magnetized quantum spin Hall insulator: monolayer 1 T′ WTe_2/$Cr_2Ge_2Te_6$. *Nat. Commun.* **13**, 5134 (2022).
39. Bauer, G. E. W., Saitoh, E. & van Wees, B. J. Spin caloritronics. *Nat. Mater.* **11**, 391–399 (2012).
40. Avci, C. O. et al. Interplay of spin-orbit torque and thermoelectric effects in ferromagnet/normal-metal bilayers. *Phys. Rev. B* **90**, 224427 (2014).
41. Xue, F., Rohmann, C., Li, J., Amin, V. & Haney, P. Unconventional spin-orbit torque in transition metal dichalcogenide–ferromagnet bilayers from first-principles calculations. *Phys. Rev. B* **102**, 014401 (2020).
42. Garcia, J. H. et al. Canted persistent spin texture and quantum spin Hall effect in WTe_2. *Phys. Rev. Lett.* **125**, 256603 (2020).
43. Zhao, W. et al. Magnetic proximity and nonreciprocal current switching in a monolayer WTe_2 helical edge. *Nat. Mater.* **19**, 503–507 (2020).
44. Snoeck, E. et al. Experimental evidence of the spin dependence of electron reflections in magnetic $CoFeO_4$/Au/Fe_3O_4 trilayers. *Phys. Rev. B* **73**, 104434 (2006).

45. Liu, G. et al. Magnonic unidirectional spin Hall magnetoresistance in a heavy-metal–ferromagnetic-insulator bilayer. *Phys. Rev. Lett.* **127**, 207206 (2021).

46. Liu, Y. et al. Field-free switching of perpendicular magnetization at room temperature using out-of-plane spins from $TaIrTe_4$. *Nat. Electron.* **6**, 732–738 (2023).

47. Kondou, K. et al. Giant field-like torque by the out-of-plane magnetic spin Hall effect in a topological antiferromagnet. *Nat. Commun.* **12**, 6491 (2021).

48. Hazra, B. K. et al. Generation of out-of-plane polarized spin current by spin swapping. *Nat. Commun.* **14**, 4549 (2023).

Methods

Device fabrication

WTe$_2$ and hexagonal boron nitride (hBN) crystals were prepared by previously published procedures[28,49]. CGT single crystals were purchased from HQ Graphene. Mechanical exfoliation of WTe$_2$, hBN, graphite and CGT was performed on separate silicon wafers with 300 nm of SiO$_2$ inside a glovebox filled with Ar gas. Flakes were selected by optical investigation using a microscope. WTe$_2$ flakes that have well-defined, straight edges were used because the a axis tends to be along straight edges[50]. For most of the devices, before heterostructure fabrication, the Pt electrodes were defined on a separate Si–SiO$_2$ substrate using electron-beam lithography and sputtering deposition with a polymethyl methacrylate resist. The electrodes contacting the heterostructure were composed of Pt (6 nm) or Ti (1–3 nm)/Pt (6–7 nm). The Pt electrodes are then connected by Cr (5 nm)/Au (110 nm) electrodes for wire-bonding pads and prepared using electron-beam lithography and electron-beam deposition with a polymethyl methacrylate/methylmethacrylate bilayer resist.

The heterostructure was fabricated using a custom transfer tool inside a glovebox filled with Ar gas. A transfer slide consisting of a polydimethylsiloxane slab and a thin film of polycarbonate was used for picking up hBN, CGT and WTe$_2$ (in that order) and then putting the stack on the Pt electrodes. For devices with a top gate, an additional graphite flake is picked up in the beginning to contact the prepatterned Pt electrodes. As for devices sandwiched between two hBN flakes, a graphite–hBN is first transferred to a Si/SiO$_2$ substrate. Pt electrodes composed of Ti (1 nm)/Pt (6 nm) were patterned on top of the hBN using electron-beam lithography and electron-beam deposition with a polymethyl methacrylate/methylmethacrylate bilayer resist. The Pt electrodes were connected to Au electrodes by the same method mentioned previously. Finally, a stack consisting of WTe$_2$–CGT–hBN was transferred on top of the Pt electrodes to complete a device. For all the UMR devices, the Pt electrodes and the substrate were cleaned by AFM in the contact mode using MikroMasch HQ:NSC15/Al BS tips and gentle oxygen plasma before the heterostructure was transferred to the electrodes to ensure good-quality electrical contacts.

Electrical measurements

The electrical measurements were performed at variable temperatures under high-vacuum (<10^{-5} mtorr) conditions. An electromagnet was rotated such that the magnetic field could be applied in both in-plane and out-of-plane directions of the device. A Keithley 6221 current source and two Keithley 2182A nanovoltmeters are used for simultaneous d.c. measurements for both transverse and longitudinal resistances. A Keithley 2400 source meter is used for applying the gate voltage to the device. For each magnetic-field hysteresis loop, the transverse and longitudinal (four-point or two-point) voltages are measured at each magnetic field when a constant d.c. charge current is applied. The antisymmetric and symmetric parts of the resistance are obtained by separately measuring the hysteresis loops at positive and negative currents. We calculate the antisymmetric and symmetric parts of the resistance as follows: $R_{xx(yx)}^{\text{symm(asym)}} = \frac{R_{xx(yx)}(+I_{\text{d.c.}}) \pm R_{xx(yx)}(-I_{\text{d.c.}})}{2}$. The voltage response that is linear (quadratic) to the current is an odd (even) function of the current, whereas the resistance ($R \equiv V/I$) of such responses will be an even (odd) function of the current. The antisymmetric (symmetric) part of the resistance will eliminate the odd (even) terms and, therefore, the linear (quadratic) current–voltage responses. We utilize this method to better quantify the observed unconventional UMR. Symmetric parts were taken for the measurements of AHE, since that will also eliminate thermal effects that are usually quadratic current responses.

Theoretical model and calculations

The Bloch electrons residing on the interface of the WTe$_2$–CGT heterostructures is minimally modelled by introducing the exchange coupling and interfacial Rashba SOC into the 1T$_d$-monolayer WTe$_2$ Hamiltonian[42] as

$$H(k_x, k_y) = \epsilon_0(k_x, k_y) + \beta \sin(k_y a_y) \sigma_0 \otimes \tau_0 + \eta \sigma_0 \otimes \tau_x + H_{\text{soc}} + H_{\text{ex}} + H_{\text{R}},$$

where $\boldsymbol{\sigma}$ and $\boldsymbol{\tau}$ are the vectors of Pauli matrices for the spin and sublattice degrees of freedom, respectively. The terms involved in the Hamiltonian read

$$\epsilon_0(k_x, k_y) = m_{\text{p}} \left[4 - 2\cos(k_x a_x) - 2\cos(k_y a_y) \right] \sigma_0 \otimes \tau_0$$
$$+ m_{\text{d}} \left[4 - 2\cos(k_x a_x) - 2\cos(k_y a_y) + \delta \right] \sigma_0 \otimes \tau_z,$$

$$H_{\text{ex}} = -\Delta_{\text{ex}} \sigma_z \otimes \tau_0,$$

$$H_{\text{R}} = -\alpha_{\text{R}} \left[\sin(k_y a_y) \sigma_x \otimes \tau_0 - \sin(k_x a_x) \sigma_y \otimes \tau_0 \right],$$

$$H_{\text{soc}} = \Lambda_x \sin(k_y a_y) \sigma_x \otimes \tau_x + \Lambda_y \sin(k_x a_x) \sigma_y \otimes \tau_x + \Lambda_z \sin(k_x a_x) \sigma_z \otimes \tau_x,$$

whose physical meaning and the specific values of the parameters are detailed in Supplementary Note 8. In particular, the Rashba term H_{R} accounts for mirror-symmetry breaking on the interface. Even though the Rashba interaction α_{R} is unknown (whereas other parameters can be obtained by fitting the band structure and the momentum-space spin texture with the density functional theory data), we notice that the UMR prevails for $\alpha_{\text{R}} \rightarrow 0$.

In the metallic regime, the extrinsic (or Fermi-surface) contribution to the first- and second-order longitudinal conductivities can be expressed as

$$\sigma_{xx}^{(1)} = e^2 \hbar \sum_n \int_{\text{BZ}} \frac{d^2\mathbf{k}}{(2\pi)^2} (v_x^{\text{nn}})^2 \frac{\Gamma^2}{\pi \left[(\epsilon_n - \mu_{\text{F}})^2 + \Gamma^2 \right]^2},$$

$$\sigma_{xx}^{(2)} = -e^3 \sum_n \int_{\text{BZ}} \frac{d^2\mathbf{k}}{(2\pi)^2} v_x^{\text{nn}} (\partial_{k_x} v_x)^{\text{nn}} \frac{\Gamma^2}{\pi \left[(\epsilon_n - \mu_{\text{F}})^2 + \Gamma^2 \right]^2},$$

where Γ represents disorder broadening, $\hbar$ is the reduced Planck constant, $v_x = \partial_{k_x} H/\hbar$ is the velocity operator with the matrix element $v_x^{nn} = \langle n|v_x|n \rangle$ and the summation runs over all the energy bands. Since the Lorentzian function $\Gamma^2/\pi[(\epsilon_n - \mu_{\text{F}})^2 + \Gamma^2]^2$ with broadening Γ is sharply centred around the chemical potential μ_{F}, only the bands near the Fermi surface are pertinent to the longitudinal conductivity. It has been argued recently that the longitudinal UMR effect is a Fermi-surface (extrinsic) effect, whereas the Fermi-sea contribution is irrelevant[51,52]. Further technical details are provided in Supplementary Note 9.

By contrast, the anomalous Hall current $j_x^{(1)} = \sigma_{xy}^{(1)} E_y$ is characterized by the linear Hall conductivity $\sigma_{xy}^{(1)}$, which is dominated by the Fermi-sea (intrinsic) contribution:

$$\sigma_{xy}^{(1)} = -2e^2 \hbar \sum_n f(\epsilon_n, \mu_{\text{F}}) \sum_{m \neq n} \int_{\text{BZ}} \frac{d^2\mathbf{k}}{(2\pi)^2} \text{Im} \left[v_y^{nm} v_x^{mn} \right] \frac{(\epsilon_n - \epsilon_m)^2 - \Gamma^2}{\left[(\epsilon_n - \epsilon_m)^2 + \Gamma^2 \right]^2},$$

where $f(\epsilon_n, \mu_{\text{F}})$ is the Fermi–Dirac distribution function. Therefore, all the occupied bands below the Fermi surface contribute to the anomalous Hall conductivity. Note that the skew scattering and side-jump mechanisms, both of which belong to the extrinsic contribution, are not included in the above formula with the approximation of the constant relaxation time $\tau = \hbar/2\Gamma$ (Supplementary Note 9).

Similarly, the non-equilibrium spin density $\delta S_\mu = \chi_{\mu\nu} E_\nu$ induced by an applied electric field can be calculated from the extrinsic (that is, intraband) contribution given by the Kubo formula:

$$\delta S_\mu = e\hbar \sum_n \int_{\text{BZ}} \frac{d^2\mathbf{k}}{(2\pi)^2} S_\mu^{\text{nn}} v_\nu^{\text{nn}} \frac{\Gamma^2}{\pi \left[(\epsilon_n - \mu_{\text{F}})^2 + \Gamma^2 \right]^2},$$

where $S = \hbar\boldsymbol{\sigma}/2$ is the spin operator. We note that for the out-of-plane spin generation δS_z (Supplementary Note 10), the intrinsic contribution is overwhelmed by the extrinsic contribution in the metallic regime if the electric field is applied along x (where the UMR is observed), whereas the opposite is true if the electric field is applied along y (where the UMR is absent). This indicates that the observed UMR is intimately related to δS_z, both of which are extrinsic and dominated by the Fermi-surface contribution. The non-equilibrium spin density as a function of the exchange field Δ_{ex} can be found in Supplementary Fig. 21. The 3×2 susceptibility $\chi_{\mu\nu}$ (no current in the z direction) characterizing the inverse spin-galvanic effect has the form

$$\chi = \begin{pmatrix} 0 & \chi_{xy} \\ \chi_{yx} & 0 \\ \chi_{zx} & 0 \end{pmatrix}.$$

For the current in the y direction ($E_x = 0$), only δS_x can be induced, which is symmetric for $\pm m_z$. However, for a current in the x direction, the non-vanishing χ_{zx} component can induce δS_z, leading to a non-vanishing UMR. Note that the susceptibility tensor $\boldsymbol{\chi}^{ISGE}$ calculated here is for our WTe$_2$–CGT device, which is different from the case of a pure WTe$_2$, owing to the exchange field from the CGT and the Rashba SOC at the interface. The former breaks the time-reversal symmetry, whereas the later breaks the inversion symmetry.

In our calculations, the parameters of exchange coupling strength, Rashba SOC, Fermi level and disorder broadening are $\Delta_{ex} = 50$ meV, $\alpha_R = 10$ meV, $E_f = 0$ and $\Gamma = 10$ meV, respectively.

Data availability
All the data supporting the findings of this study are available in the Article and its Supplementary Information. Further information is available from the corresponding author on reasonable request.

References
49. Liu, S. et al. Single crystal growth of millimeter-sized monoisotopic hexagonal boron nitride. *Chem. Mater.* **30**, 6222–6225 (2018).
50. Song, Q. et al. The polarization-dependent anisotropic Raman response of few-layer and bulk WTe$_2$ under different excitation wavelengths. *RSC Adv.* **6**, 103830–103837 (2016).
51. He, P. et al. Bilinear magnetoelectric resistance as a probe of three-dimensional spin texture in topological surface states. *Nat. Phys.* **14**, 495–499 (2018).
52. Zarezad, A. N., Barnaś, J., Qaiumzadeh, A. & Dyrdał, A. Bilinear planar Hall effect in topological insulators due to spin-momentum locking inhomogeneity. *Phys. Status Solidi RRL* **18**, 2200483 (2024).

Acknowledgements

Author contributions

Competing interests
The authors declare no competing interests.

Additional information
Supplementary information The online version contains supplementary material available at https://doi.org/10.1038/s41563-025-02175-0.

Correspondence and requests for materials should be addressed to Simranjeet Singh.

Peer review information *Nature Materials* thanks Can Onur Avci and the other, anonymous, reviewer(s) for their contribution to the peer review of this work.

Reprints and permissions information is available at www.nature.com/reprints.